Applied Numerical Mathematics 82 (2014) 32–43

Contents lists available at ScienceDirect

Applied Numerical Mathematics

www.elsevier.com/locate/apnum

An unconditionally stable hybrid method for image segmentation

Yibao Li [a], Junseok Kim [b,*]

[a] Department of Computational Science and Engineering, Yonsei University, Seoul, 120-749, Republic of Korea
[b] Department of Mathematics, Korea University, Seoul 136-713, Republic of Korea

ARTICLE INFO

Article history:
Received 8 July 2010
Received in revised form 9 September 2013
Accepted 21 December 2013
Available online 31 March 2014

Keywords:
Image segmentation
Mumford–Shah functional
Chan–Vese model
Allen–Cahn equation
Phase-field method

ABSTRACT

In this paper, we propose a new unconditionally stable hybrid numerical method for minimizing the piecewise constant Mumford–Shah functional of image segmentation. The model is based on the Allen–Cahn equation and an operator splitting technique is used to solve the model numerically. We split the governing equation into two linear equations and one nonlinear equation. One of the linear equations and the nonlinear equation are solved analytically due to the availability of closed-form solutions. The other linear equation is discretized using an implicit scheme and the resulting discrete system of equations is solved by a fast numerical algorithm such as a multigrid method. We prove the unconditional stability of the proposed scheme. Since we incorporate closed-form solutions and an unconditionally stable scheme in the solution algorithm, our proposed scheme is accurate and robust. Various numerical results on real and synthetic images with noises are presented to demonstrate the efficiency, robustness, and accuracy of the proposed method.

1. Introduction

Image segmentation is one of the fundamental tasks in automatic image analysis. Its goal is to partition a given image into regions that contain distinct objects. For example, the segmentation of structures from images is an important first step for object recognition [6], interpretation [21], image restoration [29], and image inpainting [4,7,9]. The most common form of segmentation is based on the assumption that distinct objects in an image have different and approximately constant colors. A natural approach is therefore to decompose an image domain into approximately homogeneous regions that are separated by sharp changes in image features. One of the general approaches for image segmentation is the minimizer of the piecewise constant Mumford–Shah functional [23]. Chan–Vese [10,28] solved the minimization problem by the level set method proposed by Osher and Sethian [24]. Recently, the Allen–Cahn equation [1] has been used in image segmentation [3,8,14,18,17]. In particular, Esedoḡlu and Tsai [14] used the Allen–Cahn equation to solve the reduced Mumford–Shah problem with the Chan–Vese fitting terms.

In this paper, we propose an unconditionally stable hybrid numerical method which consists of the Allen–Cahn equation and a fitting term. An operator splitting technique is used to solve the model numerically. We describe its numerical solution algorithm and give a proof of the unconditional stability of the scheme. We also present various numerical results on real

* Corresponding author.
E-mail address: cfdkim@korea.ac.kr (J. Kim).
URL: http://math.korea.ac.kr/~cfdkim (J. Kim).

http://dx.doi.org/10.1016/j.apnum.2013.12.010
0168-9274/

and synthetic images with various types and levels of noise to demonstrate the efficiency, robustness, and accuracy of the proposed numerical method.

This paper is organized as follows. In Section 2, three models for image segmentation are briefly reviewed. In Section 3, we describe the proposed unconditionally stable hybrid operator splitting method and provide a proof of the unconditional stability of the scheme. In Section 4, we perform some characteristic numerical experiments for image segmentation. Finally, conclusions are given in Section 5.

2. Description of the previous models

In this section, we briefly review three approaches such as Mumford–Shah, Chan–Vese, and phase-field models for image segmentation.

2.1. Mumford–Shah model

With a given image f_0 on the image domain Ω and its segmenting curve C, Mumford and Shah [23] proposed that the segmentation of an image can be obtained through the minimization of the following Mumford–Shah energy functional:

$$\mathcal{E}^{\mathrm{MS}}(f, C) = \mu Length(C) + \int_{\Omega} \left|f_0(\mathbf{x}) - f(\mathbf{x})\right|^2 d\mathbf{x} + \nu \int_{\Omega\setminus C} \left|\nabla f(\mathbf{x})\right|^2 d\mathbf{x},$$

where μ and ν are positive parameters and f is the piecewise smooth approximation to f_0. However, in practice it is not easy to minimize this functional because of the unknown set C of lower dimension than f.

2.2. Chan–Vese model

Chan and Vese [10] proposed an algorithm for decomposing the image into two regions with piecewise constant approximations by minimizing the energy of the Mumford and Shah functional

$$\mathcal{E}^{\mathrm{CV}}(c_1, c_2, C) = \mu Length(C) + \lambda_1 \int_{inside(C)} \left|f_0(\mathbf{x}) - c_1\right|^2 d\mathbf{x} + \lambda_2 \int_{outside(C)} \left|f_0(\mathbf{x}) - c_2\right|^2 d\mathbf{x},$$

where μ, λ_1, and λ_2 are positive parameters [15,20]. The constants c_1 and c_2 are the averages of f_0 inside and outside of C, respectively. Chan and Vese replaced the unknown curve C by the level-set function $\phi(\mathbf{x})$. Then the energy functional $\mathcal{E}^{\mathrm{CV}}(c_1, c_2, C)$ can be rewritten as

$$\begin{aligned}\mathcal{E}^{\mathrm{CV}}(c_1, c_2, \phi) = {} & \mu \int_{\Omega} \delta_\epsilon\big(\phi(\mathbf{x})\big)\left|\nabla\phi(\mathbf{x})\right| d\mathbf{x} + \lambda_1 \int_{\Omega} \left|f_0(\mathbf{x}) - c_1\right|^2 H_\epsilon\big(\phi(\mathbf{x})\big)\, d\mathbf{x} \\ & + \lambda_2 \int_{\Omega} \left|f_0(\mathbf{x}) - c_2\right|^2 \big(1 - H_\epsilon\big(\phi(\mathbf{x})\big)\big)\, d\mathbf{x}.\end{aligned}$$

By applying the gradient descent method, we obtain the following equation:

$$\frac{\partial\phi}{\partial t} = \delta_\epsilon(\phi)\left[\mu\nabla\cdot\left(\frac{\nabla\phi}{|\nabla\phi|}\right) - \lambda_1\big(f_0(\mathbf{x}) - c_1\big)^2 + \lambda_2\big(f_0(\mathbf{x}) - c_2\big)^2\right].$$

The level set based algorithm of Chan and Vese can be used to process the image with a large amount of noise and detect objects whose boundaries cannot be defined by gradient. For more details about parameters and description of equations, please refer to Ref. [10].

2.3. Phase-field model

A phase-field approximation for minimizing the Mumford–Shah functional, by using the Allen–Cahn equation to replace the length of the segmenting curve C, is given by the following energy functional:

$$\mathcal{E}(\phi) = \int_{\Omega} \left(\frac{F(\phi)}{\epsilon^2} + \frac{|\nabla\phi|^2}{2} + G(\phi, f_0)\right) d\mathbf{x}, \tag{1}$$

where $F(\phi) = 0.25(\phi^2 - 1)^2$ is a double-well potential as shown in Fig. 1, ϵ is the gradient energy coefficient related to the interfacial energy, and Ω is the image domain.

When ϕ is locally equilibrated, the first two terms in Eq. (1) are proportional to the length of the segmenting curve C [12] by

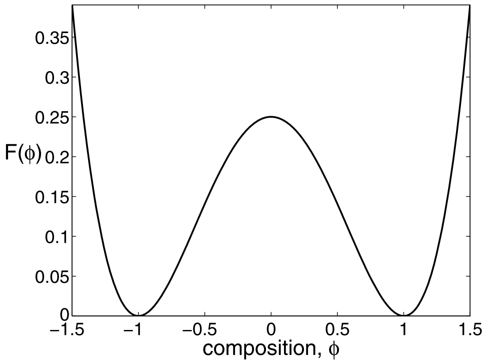

Fig. 1. A double well potential, $F(\phi) = 0.25(\phi^2 - 1)^2$.

$$\int_\Omega \left(\frac{F(\phi)}{\epsilon^2} + \frac{|\nabla \phi|^2}{2} \right) d\mathbf{x} \approx \frac{2\sqrt{2}}{3\epsilon} Length(C).$$

The third term in the functional is the fitting term and defined as

$$G(\phi, f_0) = \frac{\lambda}{2}\left[(1+\phi)^2 (f_0 - c_1)^2 + (1-\phi)^2 (f_0 - c_2)^2 \right].$$

Here, the fitting term plays a key role in curve evolution by making the phase-field resemble the original image shape, λ is a nonnegative parameter and f_0 is the given image. Also c_1 and c_2 are the averages of f_0 in the regions ($\phi \geqslant 0$) and ($\phi < 0$), respectively:

$$c_1 = \frac{\int_\Omega f_0(\mathbf{x})(1+\phi(\mathbf{x}))\, d\mathbf{x}}{\int_\Omega (1+\phi(\mathbf{x}))\, d\mathbf{x}} \quad \text{and} \quad c_2 = \frac{\int_\Omega f_0(\mathbf{x})(1-\phi(\mathbf{x}))\, d\mathbf{x}}{\int_\Omega (1-\phi(\mathbf{x}))\, d\mathbf{x}}.$$

Once ϕ reaches a steady state, the zero level set of ϕ becomes the contour that separates the object from the background. For this purpose, we seek a law of evolution in the form [11]: $\phi_t = -\nabla \mathcal{E}(\phi)$. The symbol '$\nabla$' here denotes the gradient in the space $L^2(\Omega)$. Let $\phi, \varphi \in D = \{c \in H^2(\Omega) \mid \frac{\partial c}{\partial n} = 0 \text{ on } \partial\Omega\}$. Then, we have

$$\begin{aligned} \left(\nabla \mathcal{E}(\phi), \varphi\right)_{L^2} &= \lim_{h \to 0} \frac{\mathcal{E}(\phi + h\varphi) - \mathcal{E}(\phi)}{h} \\ &= \int_\Omega \left(\frac{F'(\phi)}{\epsilon^2} - \Delta\phi + \lambda\left[(1+\phi)(f_0 - c_1)^2 - (1-\phi)(f_0 - c_2)^2 \right] \right) \varphi \, d\mathbf{x} \\ &= \left(\frac{F'(\phi)}{\epsilon^2} - \Delta\phi + \lambda\left[(1+\phi)(f_0 - c_1)^2 - (1-\phi)(f_0 - c_2)^2 \right], \varphi \right)_{L^2}. \end{aligned}$$

Therefore, we get the following gradient descent flow equation:

$$\phi_t = -\frac{F'(\phi)}{\epsilon^2} + \Delta\phi + \lambda\left[(1-\phi)(f_0 - c_2)^2 - (1+\phi)(f_0 - c_1)^2 \right]. \tag{2}$$

In Eq. (2), $\phi_t = -F'(\phi)/\epsilon^2 + \Delta\phi$ is the Allen–Cahn equation which approximates motion by mean curvature of the interface that separates -1 and 1 phases of the solutions [14]. Therefore, depending on the sign of the term $\lambda[(1-\phi)(f_0 - c_2)^2 - (1+\phi)(f_0 - c_1)^2]$, the interface shrinks or expands to become the segmentation curve.

3. Numerical solution

In this section, we describe a new unconditionally stable hybrid numerical method for minimizing the piecewise constant Mumford–Shah functional of image segmentation. Using an operator splitting technique, we split its numerical solution algorithm into two linear equations and one nonlinear equation. One linear equation and the nonlinear equation are solved analytically. The other linear equation is discretized using an implicit scheme and the resulting discrete system of equations is solved by a multigrid method. We prove the unconditionally stable property of the proposed scheme by analysis.

3.1. Proposed numerical scheme

Eq. (2) is discretized in a two-dimensional space $\Omega = (a, b) \times (c, d)$. Let N_x and N_y be positive even integers, $h = (b-a)/N_x$ be the uniform mesh size, and $\Omega_h = \{(x_i, y_j)\colon\ x_i = (i-0.5)h,\ y_j = (j-0.5)h,\ 1 \leqslant i \leqslant N_x,\ 1 \leqslant j \leqslant N_y\}$ be the set of cell-centers. Let ϕ_{ij}^n be approximations of $\phi(x_i, y_j, n\Delta t)$, where $\Delta t = T/N_t$ is the time step, T is the final time, and N_t is the total number of time steps. Using the standard five point stencil for the discrete Laplacian $\Delta_d \phi_{ij} = (\phi_{i-1,j} + \phi_{i+1,j} - 4\phi_{ij} + \phi_{i,j-1} + \phi_{i,j+1})/h^2$, we propose the following operator splitting numerical algorithm:

$$\frac{\phi_{ij}^{n+1} - \phi_{ij}^n}{\Delta t} = -\frac{F'(\phi_{ij}^{n+1})}{\epsilon^2} + \Delta_d \phi_{ij}^{n+1,2} + \lambda\big[\big(1-\phi_{ij}^{n+1,1}\big)\big(f_{0,ij} - c_2^n\big)^2 - \big(1+\phi_{ij}^{n+1,1}\big)\big(f_{0,ij} - c_1^n\big)^2\big],$$

where $F'(\phi) = \phi(\phi^2 - 1)$ and $\phi_{ij}^{n+1,k}$ for $k = 1, 2$ are defined in the following operator splitting scheme.

$$\frac{\phi_{ij}^{n+1,1} - \phi_{ij}^n}{\Delta t} = \lambda\big[\big(1-\phi_{ij}^{n+1,1}\big)\big(f_{0,ij} - c_2^n\big)^2 - \big(1+\phi_{ij}^{n+1,1}\big)\big(f_{0,ij} - c_1^n\big)^2\big], \tag{3}$$

$$\frac{\phi_{ij}^{n+1,2} - \phi_{ij}^{n+1,1}}{\Delta t} = \Delta_d \phi_{ij}^{n+1,2}, \tag{4}$$

$$\frac{\phi_{ij}^{n+1} - \phi_{ij}^{n+1,2}}{\Delta t} = -\frac{F'(\phi_{ij}^{n+1})}{\epsilon^2}, \tag{5}$$

where c_1^n and c_2^n are

$$c_1^n = \frac{\sum_{i=1}^{N_x}\sum_{j=1}^{N_y} f_{0,ij}(1+\phi_{ij}^n)}{\sum_{i=1}^{N_x}\sum_{j=1}^{N_y}(1+\phi_{ij}^n)} \quad \text{and} \quad c_2^n = \frac{\sum_{i=1}^{N_x}\sum_{j=1}^{N_y} f_{0,ij}(1-\phi_{ij}^n)}{\sum_{i=1}^{N_x}\sum_{j=1}^{N_y}(1-\phi_{ij}^n)}.$$

We can consider Eq. (3) is an approximation of the equation

$$\phi_t = -\lambda\big[(f_0 - c_1)^2 + (f_0 - c_2)^2\big]\phi - \lambda\big[(f_0 - c_1)^2 - (f_0 - c_2)^2\big] \tag{6}$$

by the implicit Euler method with the initial condition ϕ^n. We can solve Eq. (6) analytically since it is a first-order linear differential equation and the solution after Δt is given as

$$\phi_{ij}^{n+1,1} = e^{-\lambda[(f_0-c_1^n)^2+(f_0-c_2^n)^2]\Delta t}\phi_{ij}^n + \big(e^{-\lambda[(f_0-c_1^n)^2+(f_0-c_2^n)^2]\Delta t} - 1\big)\frac{(f_0 - c_1^n)^2 - (f_0 - c_2^n)^2}{(f_0 - c_1^n)^2 + (f_0 - c_2^n)^2}.$$

Next Eq. (4) is the implicit Euler scheme and can be solved by a multigrid method [5,27] with the initial condition $\phi^{n+1,1}$. Finally we can consider Eq. (5) as an approximation of the equation

$$\phi_t = \frac{(\phi - \phi^3)}{\epsilon^2} \tag{7}$$

by an implicit Euler method with the initial condition $\phi^{n+1,2}$. Then the solution of Eq. (7) after Δt, solved by the method of separation of variables [16,26], is given as $\phi^{n+1} = \phi^{n+1,2}/\sqrt{e^{-2\Delta t/\epsilon^2} + (\phi^{n+1,2})^2(1 - e^{-2\Delta t/\epsilon^2})}$. Finally, our proposed scheme is written as

$$\phi^{n+1,1} = e^{-\lambda[(f_0-c_1^n)^2+(f_0-c_2^n)^2]\Delta t}\phi^n + \big(e^{-\lambda[(f_0-c_1^n)^2+(f_0-c_2^n)^2]\Delta t} - 1\big)\frac{(f_0 - c_1^n)^2 - (f_0 - c_2^n)^2}{(f_0 - c_1^n)^2 + (f_0 - c_2^n)^2}, \tag{8}$$

$$\frac{\phi^{n+1,2} - \phi^{n+1,1}}{\Delta t} = \Delta_d \phi^{n+1,2}, \tag{9}$$

$$\phi^{n+1} = \frac{\phi^{n+1,2}}{\sqrt{e^{\frac{-2\Delta t}{\epsilon^2}} + (\phi^{n+1,2})^2(1 - e^{\frac{-2\Delta t}{\epsilon^2}})}}. \tag{10}$$

The solutions of Eqs. (8) and (10) are explicitly defined. Eq. (9) is a heat equation and we apply a fast solver such as a multigrid method to solve the equation.

3.2. Stability analysis for the proposed scheme

When we solve time-dependent partial differential equations, stability of the numerical scheme to the equations is very important. Explicit time integration schemes are generally only conditionally stable and require small time steps to be employed to insure numerical stability. Therefore, the step size restriction is often more severe than accuracy considerations require. However, since our proposed hybrid splitting method is unconditionally stable we do not have time step restrictions. Next we prove the unconditional stability of the scheme. For simplicity, let us define

$$\alpha = e^{-\lambda[(f-c_1^n)^2+(f-c_2^n)^2]\Delta t} \quad \text{and} \quad \beta = \frac{(f_0-c_1^n)^2-(f_0-c_2^n)^2}{(f_0-c_1^n)^2+(f_0-c_2^n)^2}.$$

Then, Eq. (8) can be rewritten as $\phi^{n+1,1} = \alpha\phi^n + (\alpha-1)\beta$. Now, we get

$$\left|\phi^{n+1,1}\right| \leqslant \alpha\left|\phi^n\right| + (1-\alpha)|\beta| \leqslant \alpha + 1 - \alpha = 1. \tag{11}$$

Here we have used $0 < \alpha \leqslant 1$, $|\beta| \leqslant 1$, and $|\phi^n| \leqslant 1$. For Eq. (9), a von Neumann stability analysis [13] shows that an implicit Euler method is unconditionally stable. The inequality $|\phi^{n+1,2}| \leqslant \|\phi^{n+1,1}\|_\infty$ is satisfied by the discrete maximum principle for the heat equation [22]. Then by Eq. (11), we get $|\phi^{n+1,2}| \leqslant 1$. Finally, from Eq. (10), we have

$$\left|\phi^{n+1}\right| = \frac{|\phi^{n+1,2}|}{\sqrt{e^{\frac{-2\Delta t}{\epsilon^2}} + (\phi^{n+1,2})^2(1-e^{\frac{-2\Delta t}{\epsilon^2}})}} = \frac{1}{\sqrt{1+(\frac{1}{(\phi^{n+1,2})^2}-1)e^{\frac{-2\Delta t}{\epsilon^2}}}} \leqslant 1.$$

Hence, if $|\phi^n| \leqslant 1$, then we get $|\phi^{n+1}| \leqslant 1$. Therefore the proposed scheme is unconditionally stable for any time step. And we also define the numerical quadrature for the energy functional, Eq. (1).

$$\mathcal{E}(\phi) = \sum_{i=1}^{N_x}\sum_{j=1}^{N_y} h^2\left(\frac{F(\phi_{ij})}{\epsilon^2} + \frac{|\nabla_d\phi_{ij}|^2}{2} + \frac{\lambda}{2}(1+\phi_{ij})^2(f_{0,ij}-c_1)^2 + \frac{\lambda}{2}(1-\phi_{ij})^2(f_{0,ij}-c_2)^2\right).$$

4. Experimental results

In this section, we present numerical results using the proposed numerical algorithm on various synthetic and real images. We show that a very fast and accurate minimization can be achieved by the proposed algorithm. In our numerical experiments, we normalize the given image f as $f_0 = \frac{f-f_{min}}{f_{max}-f_{min}}$, where f_{max} and f_{min} are the maximum and the minimum values of the given image, respectively. Across the interfacial regions, the phase-field varies from -0.9 to 0.9 over a distance of approximately $2\sqrt{2}\epsilon\tanh^{-1}(0.9)$. Therefore, if we want this value to be approximately m grid points, then the ϵ value needs to be taken as follows: $\epsilon_m = hm/[2\sqrt{2}\tanh^{-1}(0.9)]$. Since solutions with the proposed numerical scheme are almost insensitive to the initial configuration of ϕ^0, we simply initialize $\phi^0 = 2f_0 - 1$. We stop the numerical computations when the difference between the $(n+1)$th and nth time step energies becomes less than a given tolerance, *tol*. The termination criterion algorithm is listed as follows:

Set a maximum iteration number N, a tolerance *tol*, and $k = 1$.
While $(k \leqslant N)$ do *Steps 1–2*
Step 1 Compute ϕ^{n+1} from ϕ^n by solving Eqs. (8)–(10).
Step 2 If $|\mathcal{E}(\phi^{n+1}) - \mathcal{E}(\phi^n)| < tol$, then stop the calculation.
Else $k = k + 1$.

4.1. The basic mechanism of the algorithm

We start with an example which shows the basic mechanism of the algorithm, Eq. (2). Let us consider a synthetic image on the computational domain, $\Omega = (0,1)\times(0,1)$: $f(x,y) = \frac{1}{2}[1+\tanh(\frac{0.2-\sqrt{(x-0.4)^2+(y-0.5)^2}}{\sqrt{2}\epsilon_5})]$. This image is shown in the first row in Fig. 2. White region is close to 1 and gray region is close to 0. Let an initial phase-field ϕ^0 as $\phi^0(x,y) = \tanh(\frac{0.2-\sqrt{(x-0.6)^2+(y-0.5)^2}}{\sqrt{2}\epsilon_5})$, which is shown in the second row in Fig. 2(a). A 64×64 grid, interface parameter ϵ_5, time step $\Delta t = 1\text{E}{-4}$, $tol = 0.2$, and $\lambda = 8\text{E}3$ are used.

The top row shows the evolving contours overlaid on the original image. The middle and bottom rows show the evolution of ϕ with its zero level set and the fitting term in Eq. (3), i.e., $\lambda[(1-\phi^{n+1,1})(f_0-c_2^n)^2 - (1+\phi^{n+1,1})(f_0-c_1^n)^2]$, respectively. Columns (a), (b), (c), and (d) are at $n = 0$, 1, 3, and 10, respectively. From the results in Fig. 2, we observe that the positive and negative values of the fitting term imply that ϕ will increase and decrease until the segmentation curve is on the edge of the object, respectively. Note that in the third row of Fig. 2(d), the value of fitting term is positive and negative inside and outside of the disk, respectively. This makes the segmentation evolution reach a steady state.

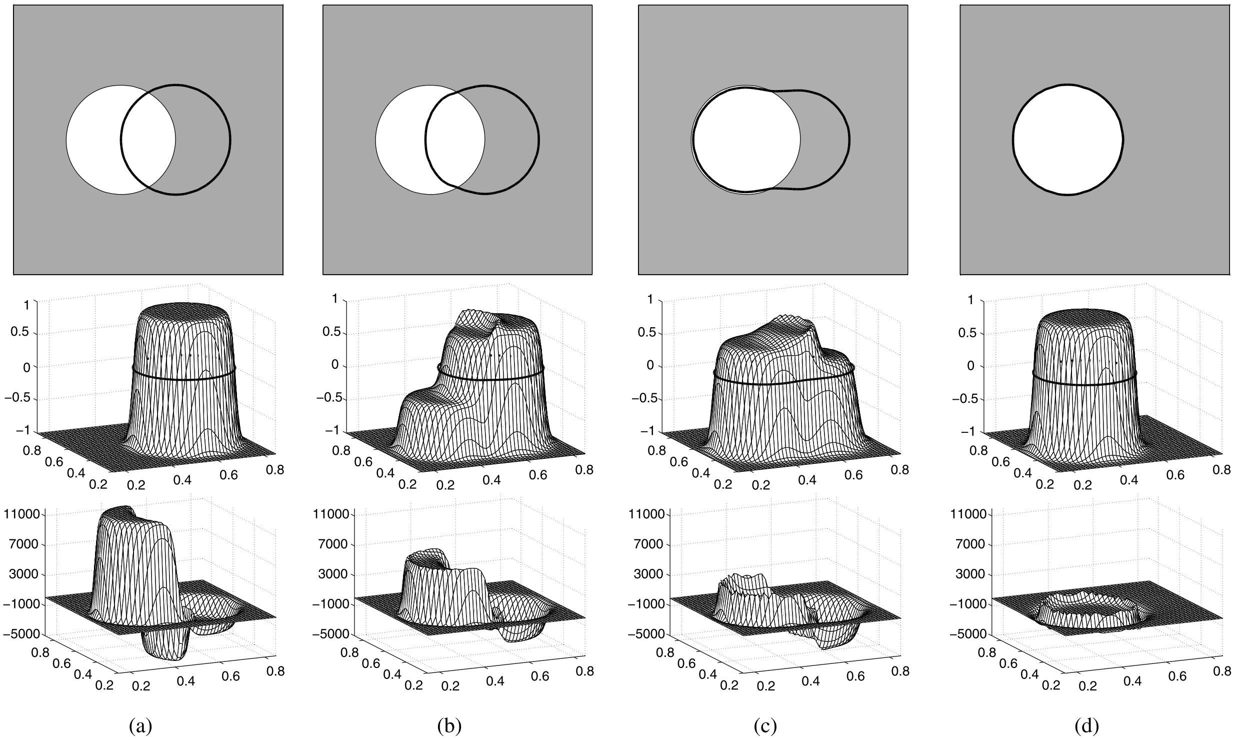

Fig. 2. Synthetic image segmentation using the proposed method. Top: the evolution of the zero level set of ϕ is presented. Middle: the evolution of ϕ and its zero level set. Bottom: the evolution of the right hand side term in Eq. (3), $\lambda[(1-\phi^{n+1,1})(f_0-c_2^n)^2-(1+\phi^{n+1,1})(f_0-c_1^n)^2]$ is shown. Columns (a), (b), (c), and (d) are at $n=0,1,3$, and 10, respectively.

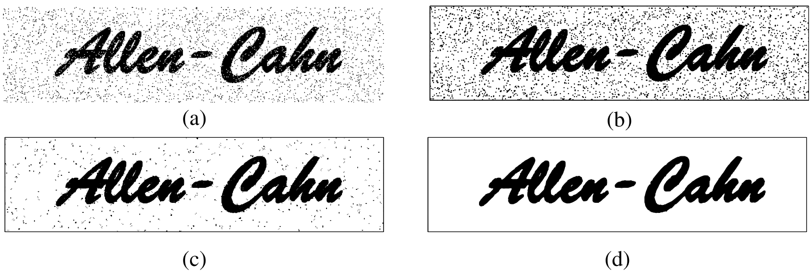

Fig. 3. (a) Original image with 10% salt-and-pepper noise. (b), (c), and (d) are zero level filled contours at times $t=0$, 2E–5 (1 iteration), and 8E–5 (4 iterations), respectively. Interface parameter ϵ_8, $\Delta t=$ 2E–5, and $\lambda=$ 1E4 are used.

4.2. Salt-and-pepper noise

Fig. 3(a) is a text image 'Allen–Cahn' with 'Brush Script MT' font and blurred with 10% salt-and-pepper noise [2] on the computational domain, $\Omega=(0,4)\times(0,1)$ with a 512×128 mesh. Interface parameter ϵ_8, $\Delta t=$ 2E–5, $tol=0.2$, and $\lambda=$ 1E4 are used. Salt-and-pepper noise is defined as randomly occurring white and black pixels. The given probability r% means setting a fraction of $(r/2)$% randomly selected pixels to black and the other $(r/2)$% randomly to white. Figs. 3(b), (c), and (d) are zero level filled contours at times $t=0$, 2E–5 (1 iteration), and 8E–5 (4 iterations), respectively. We also note that we can segment the enclosed holes in the letters.

Fig. 4 is an image segmentation for a fingerprint on the computational domain $\Omega=(0,1)\times(0,1)$ with a 256×256 mesh. Interface parameter ϵ_3, time step $\Delta t=$ 5E–6, $tol=0.25$, and $\lambda=$ 1.5E5 are used. We can observe that the proposed model fully segments the image after 10 iterations.

4.3. Gray-scale noise

Fig. 5 shows characters with gray-scale noises. r% gray-scale noise means that r% of the pixels in the image are replaced with random numbers chosen from a uniform distribution between 0 and 1. The computational domain is set to $\Omega=(0,4)\times(0,1)$ with a 512×128 mesh. Interface parameter ϵ_6, time step $\Delta t=$ 5E–5, $tol=0.25$, and $\lambda=$ 5E3 are used. The

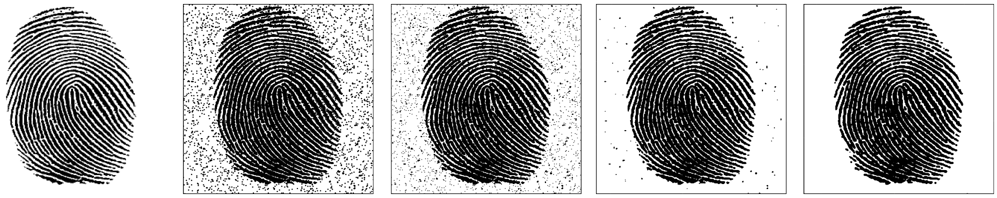

(a) (b) (c) (d) (e)

Fig. 4. Finger print. (a) Initial image, (b) 10% salt-and-pepper noise is superposed over the original image, (c) $t = 4\text{E}{-}6$ (2 iterations), (d) $t = 8\text{E}{-}6$ (4 iterations), and (e) $t = 2\text{E}{-}5$ (10 iterations).

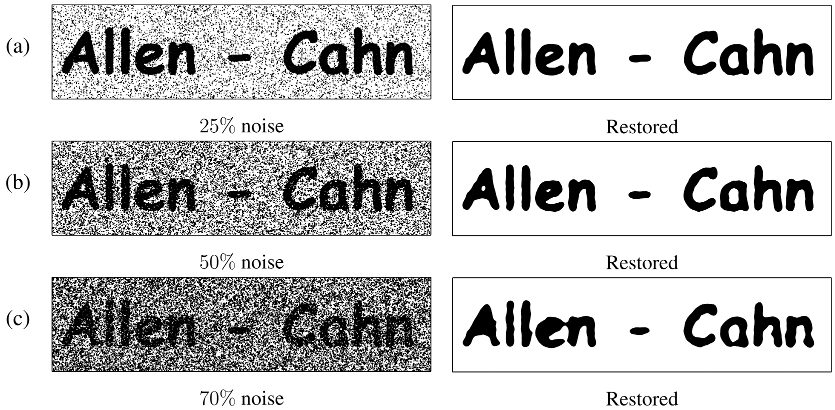

Fig. 5. The first column is the original images with gray-scale noises 25%, 50%, and 70% from top to bottom, respectively. The second column is the restored images with 5, 7, and 9 iterations from top to bottom, respectively.

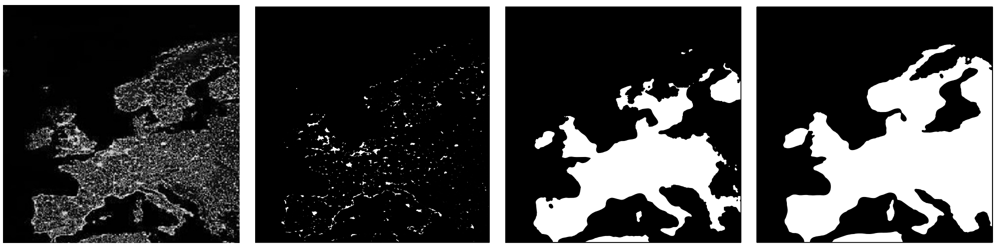

(a) (b) (c) (d)

Fig. 6. Europe night-lights. (a) initial image, (b) contour of the initial image, (c) $t = 2.5\text{E}{-}4$ (2 iterations), and (d) $t = 1.375\text{E}{-}3$ (11 iterations). Image source: NASA/Goddard Space Flight Center Scientific Visualization Studio (http://svs.gsfc.nasa.gov/vis/a000000/a002200/a002276/index.html).

left column consists of the original images with 25%, 50%, and 70% noises from top to bottom and the right column is their restored images. The proposed model successfully segments the images with 25% and 50% gray-scale noises. Even the 70% noise-blurred image can be segmented well.

4.4. Contours without gradient

In this example, we show that our proposed model can be used to detect cognitive contours from objects which cannot be defined by a gradient. We want to test our method on a very challenging image with scattered data such as a satellite image of Europe showing clusters of light. In Fig. 6, the segmentation of Europe night-lights is shown. The computational domain is set to $\Omega = (0, 1) \times (0, 1)$ with a 256×256 mesh. Interface parameter ϵ_{100}, time step $\Delta t = 1.25\text{E}{-}4$, $tol = 10$, and $\lambda = 1.5\text{E}5$ are used. The method produces visually clear results. It only took 11 iterations, which is one order of magnitude smaller than the previous methods [10,18].

4.5. Blood vessel image

Fig. 7 shows the segmentation results for a real blood vessel (left anterior descending) image with inhomogeneous intensity via use of the proposed numerical method. The computational domain is set to $\Omega = (0, 1) \times (0, 1)$ with a 64×64

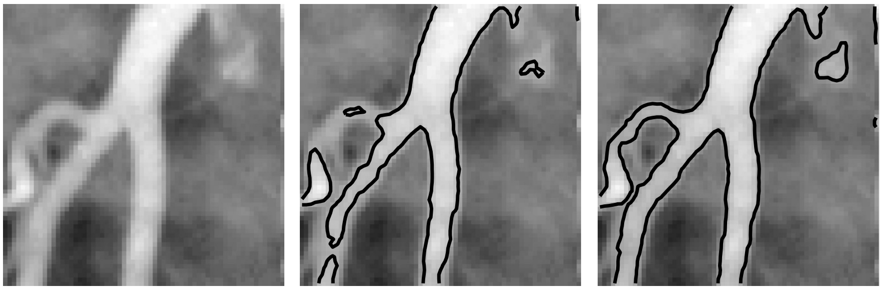

(a) 0 iteration (b) 8 iterations (c) 16 iterations

Fig. 7. The image with the left anterior descending vessel. The iteration numbers are shown below each figure.

(a) (b) (c) (d)

Fig. 8. Segmentation of the image for a solid brain tumor. (a) Initial image, (b) contour of the initial image, (c) contour the image (20 iterations), and (d) contour is superposed over the initial image to show the accuracy.

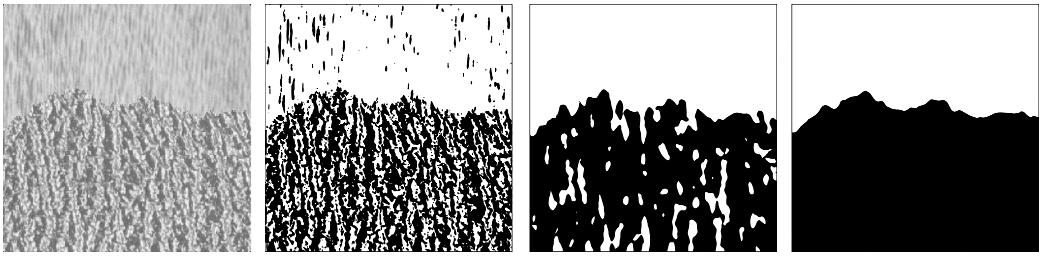

(a) (b) (c) (d)

Fig. 9. Texture image. (a) Initial image, (b) contour of initial image, (c) $t = 2\text{E}{-}4$ (2 iterations), and (d) $t = 6\text{E}{-}4$ (6 iterations).

mesh. Interface parameter ϵ_5, time step $\Delta t = 1.6\text{E}{-}6$, $tol = 0.2$, and $\lambda = 2\text{E}5$ are used. It can be seen from Fig. 7(c) that the image is successfully segmented after 16 iterations.

4.6. Brain MR image

We show that our proposed model can be used to analyze medical images to provide necessary and useful information for medical treatment. In Fig. 8, the segmentations of brain MR image are shown on the computational domain $\Omega = (0,1) \times (0,1)$ with a 256×256 mesh. Interface parameter ϵ_5, time step $\Delta t = 5\text{E}{-}6$, $tol = 0.05$, and $\lambda = 1\text{E}4$ are used. As can be observed from Fig. 8(d), the agreement between the area of the brain solid tumor and the segmentation of image is good.

4.7. Texture image

Texture image, based on local spatial variations of intensity or color to identify these types of homogeneous image regions, is an important attribute used in image analysis and pattern recognition. Fig. 9 shows that our proposed model can be very useful in detecting texture image segmentation. The computational domain is set to $\Omega = (0,1) \times (0,1)$ with a 256×256 mesh. Interface parameter ϵ_{50}, time step $\Delta t = 1\text{E}{-}4$, $tol = 1$, and $\lambda = 1\text{E}4$ are used. As can be seen, our proposed method has performed well in texture image segmentation. Another test is performed to compare with a well-known model [19], in which the authors provided a general algorithm for partitioning grayscale images into disjoint regions of coherent brightness and texture. Here a 256×384 mesh grid is used on the computational domain $\Omega = (0,1) \times (0,1.5)$. And other

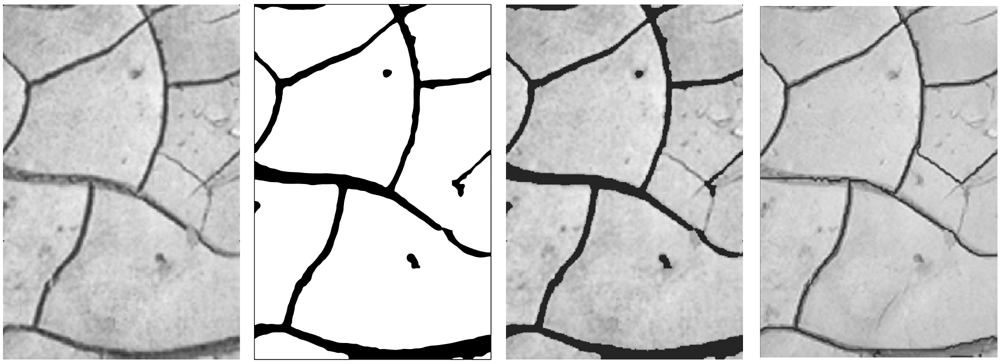

(a) (b) (c) (d)

Fig. 10. Texture image. (a) Initial image, (b) contour of the segmented image (10 iterations), (c) overlapped simulation by comparing the initial image, and (d) the results obtained by Malik et al. [19].
Figure reprinted with permission from Malik et al., Int. J. Comput. Vis., 43 (2001) 7–27 [19].

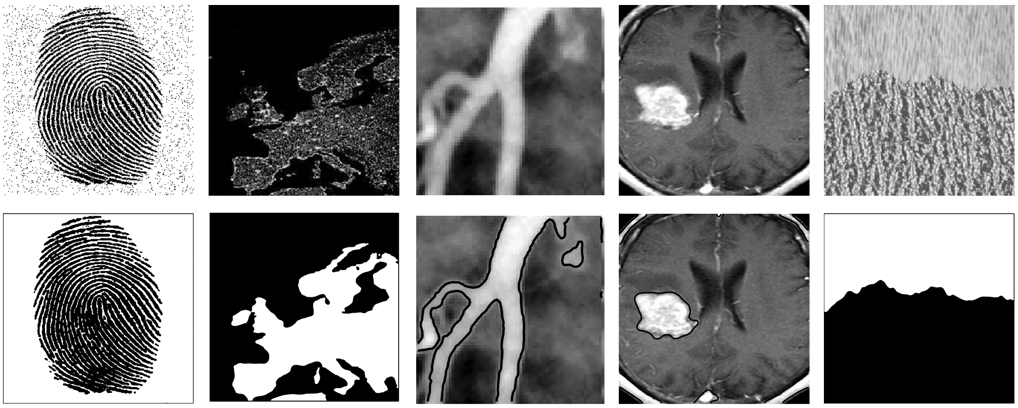

(a) (b) (c) (d) (e)

Fig. 11. The top row shows original images and the bottom row shows the segmented results.

Table 1
The performance of our proposed method in segmenting images in Fig. 11.

Case	(a)	(b)	(c)	(d)	(e)
Image size	256 × 256	256 × 256	64 × 64	256 × 256	256 × 256
Iterations	4	11	16	20	6
CPU time (s)	0.250	0.687	0.015	0.967	0.406

parameters are chosen as ϵ_{10}, $\Delta t = 1\text{E}{-}4$, $tol = 20$, and $\lambda = 5\text{E}5$. The image is successfully segmented after 10 iterations as shown in Figs. 10(b) and (c). In Fig. 10(d), we show the result which is obtained by the previous work [19]. As can be observed that both of two methods perform well to segment texture image. While our method is to partition the image into several regions and segment the texture image. On the other hand, Malik et al.'s model works by using a gating operator based on the texturedness of the neighborhood at a pixel.

4.8. Computational cost

Next, we show the performance of the five test problems which were conducted in previous sections (see Fig. 11 and Table 1). Tests were performed on a 3.4 GHz Intel Pentium with 3.4 GB of RAM. Since our algorithm consists of two explicit evaluations of the closed-form solutions and one implicit heat equation solver, we can expect both accuracy and efficiency. For the heat equation solver, we apply a multigrid method which was used in [25] for geometric active contour problems successfully. The image sizes, the iteration numbers, and the CPU times in Fig. 11 are listed in Table 1. In most cases, the number of iterations is relatively small.

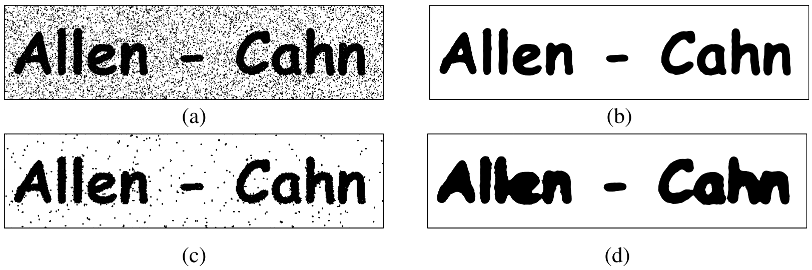

Fig. 12. Parameter sensitivity analysis for ϵ. (a) Original image, (b) segmented image with ϵ_6, (c) segmented image with ϵ_1, and (b) segmented image with ϵ_{15}.

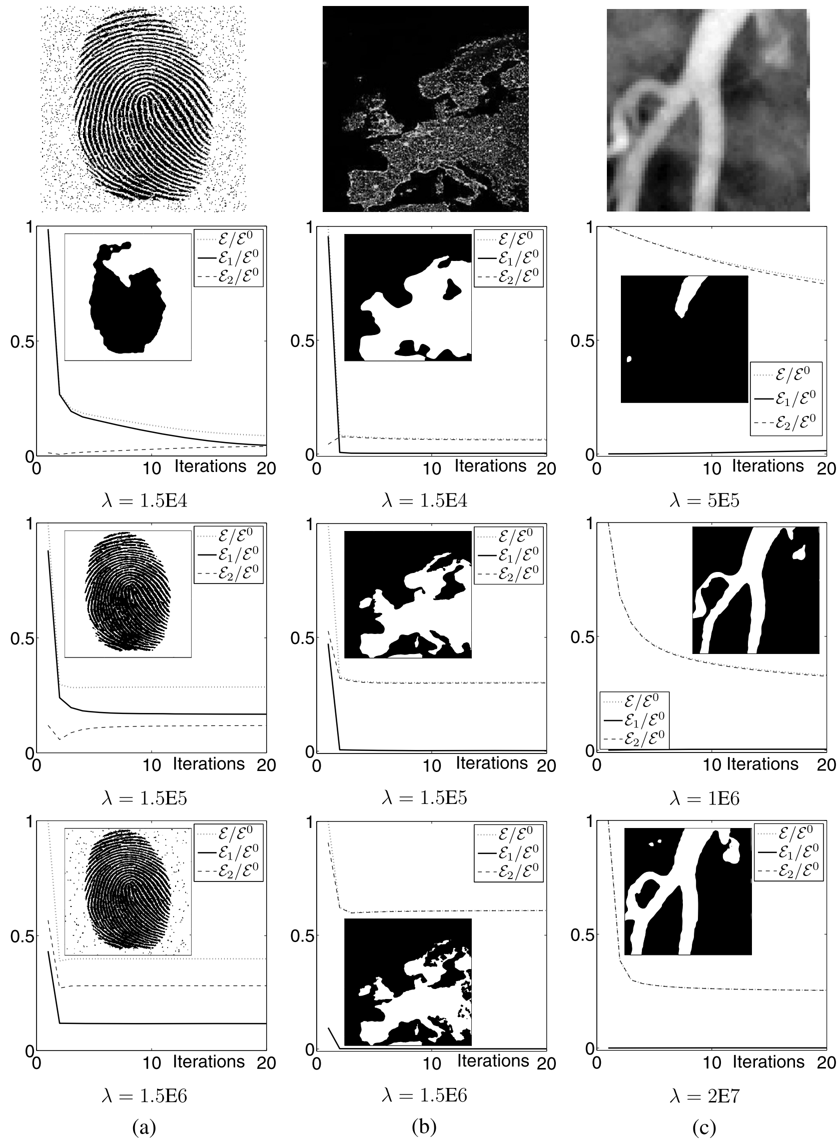

Fig. 13. Comparison of segmented image and energy functional with different λ. Here $\mathcal{E}^0$ is the total energy functional $\mathcal{E}$ at initial time. The chosen λ values are listed below each figure. (a) Finger print, (b) Europe night-lights, and (c) left anterior descending vessel.

4.9. Parameter sensitivity analysis

Finally, we perform parameter sensitivity analysis for the model parameters ϵ and λ. First, we take the image from Fig. 5(a) and investigate the effect of parameter ϵ on the results. The time step size is taken as $\Delta t = 1\text{E}{-}5$. Fig. 12(b), (c), and (d) are results with ϵ_6, ϵ_1, and ϵ_{15}, respectively. Here $\lambda = 5\text{E}3$ is used. When ϵ is too small, then small clusters cannot be removed effectively. On the other hand, if ϵ is too large, then the restored letters become so much fatter.

Next we investigate the effect of parameter λ on the results. Before that, let us denote $\mathcal{E}_1 = \int_\Omega (F(\phi)/\epsilon^2 + |\nabla\phi|^2/2)\, d\mathbf{x}$ and $\mathcal{E}_2 = \int_\Omega G(\phi, f_0)\, d\mathbf{x}$. Thus our proposed functional can be written as $\mathcal{E} = \mathcal{E}_1 + \mathcal{E}_2$. Fig. 13 shows the comparison of segmented image and energy functionals ($\mathcal{E}$, $\mathcal{E}_1$, $\mathcal{E}_2$) with different λ. The chosen λ values are listed below each figure. For all the cases, the total energy functionals are decreasing. In general, when λ is too small, then motion by the mean curvature flow is dominant. On the other hand, if λ is too large, then the fitting term is dominant and the restored image tends to become the original image with noise.

5. Conclusion

In this paper, we proposed an unconditionally stable hybrid numerical scheme for minimizing the problems associated with the piecewise constant Mumford–Shah functional of image segmentation. The model and its numerical scheme are based on the Allen–Cahn equation and an operator splitting technique, respectively. We described the numerical solution algorithm and gave the proof of the unconditional stability of the numerical scheme. Finally various experimental results on real and synthetic images with noise were presented to demonstrate the accuracy and efficiency of the proposed method. It should be pointed that our proposed model is a modified version of Chan and Vese's model, which is a powerful method that can successfully segment many types of images, including some that would be difficult to segment with gradient-based methods. While Chan and Vese's model fails to detect the certain images which have edges and poor image quality. In our proposed method, there is a parameter λ which should be chosen by trial and error. In our future work, we will classify images and find an automatic decision of the range of λ values according to image features.

Acknowledgements

This research was supported by Basic Science Research Program through the National Research Foundation of Korea (NRF) funded by the Ministry of Education, Science and Technology (No. 2009-0074248). The authors also wish to thank the reviewers for the constructive and helpful comments on the revision of this article.

References

[1] S.M. Allen, J.W. Cahn, A microscopic theory for antiphase boundary motion and its application to antiphase domain coarsening, Acta Metall. 27 (1979) 1085–1095.
[2] G.R. Arce, J.L. Paredes, J. Mullan, Nonlinear filtering for image analysis and enhancement, in: Handbook of Image and Video Processing, Academic Press, 2000.
[3] M. Beneš, V. Chalupecký, K. Mikula, Geometrical image segmentation by the Allen–Cahn equation, Appl. Numer. Math. 51 (2–3) (2004) 187–205.
[4] M. Bertalmio, G. Sapiro, V. Caselles, C. Ballester, Image inpainting, in: Proceedings of SIGGRAPH 2000, New Orleans, 2000.
[5] W.L. Briggs, A Multigrid Tutorial, SIAM, Philadelphia, 1987.
[6] V.G. Brunet, B. Lameyre, Object recognition and segmentation in videos by connecting heterogeneous visual features, Comput. Vis. Image Underst. 111 (1) (2008) 86–109.
[7] M. Burger, L. He, C. Schöenlieb, Cahn–Hilliard inpainting and a generalization for grayvalue images, UCLA CAM report 08, 2008.
[8] T.F. Chan, S. Esedoḡlu, M. Nikolova, Algorithms for finding global minimizers of image segmentation and denoising models, SIAM J. Appl. Math. 66 (5) (2006) 1632–1648.
[9] T.F. Chan, J. Shen, Mathematical models for local non-texture inpaintings, SIAM J. Appl. Math. 62 (2002) 1019–1043.
[10] T. Chan, L. Vese, Active contours without edges, IEEE Trans. Image Process. 10 (2) (2001) 266–277.
[11] C. Cowan, The Cahn–Hilliard equation as a gradient flow, M.S. Thesis, Simon Fraser University, Canada, 2005.
[12] Q. Du, C. Liu, X. Wang, A phase field approach in the numerical study of the elastic bending energy for vesicle membranes, J. Comput. Phys. 198 (2004) 450–468.
[13] D.J. Duffy, Finite Difference Methods in Financial Engineering: A Partial Differential Equation Approach, Wiley Finance Series, 2006.
[14] S. Esedoḡlu, Y.H.R. Tsai, Threshold dynamics for the piecewise constant Mumford–Shah functional, J. Comput. Phys. 211 (1) (2006) 367–384.
[15] A. Goshtasby, M. Satter, An adaptive window mechanism for image smoothing, Comput. Vis. Image Underst. 111 (2) (2008) 155–169.
[16] Y. Li, H.G. Lee, D. Jeong, J.S. Kim, An unconditionally stable hybrid numerical method for solving the Allen–Cahn equation, Comput. Math. Appl. 60 (2010) 1591–1606.
[17] Y. Li, J.S. Kim, Multiphase image segmentation using a phase-field model, Comput. Math. Appl. 62 (2011) 737–745.
[18] J. Lie, M. Lysaker, X.C. Tai, A binary level set model and some applications to Mumford–Shah image segmentation, IEEE Trans. Image Process. 15 (5) (2006) 1171–1181.
[19] J. Malik, S. Belongie, T. Leung, J. Shi, Contour and texture analysis for image segmentation, Int. J. Comput. Vis. 43 (1) (2001) 7–27.
[20] J. Mille, Narrow band region-based active contours and surfaces for 2D and 3D segmentation, Comput. Vis. Image Underst. 113 (9) (2009) 946–965.
[21] J.M. Morel, S. Solimini, Variational Methods in Image Segmentation, Prog. Nonlinear Differ. Equ. Appl., Birkhäuser, Boston, MA, 1995.
[22] K.W. Morton, D.E. Mayers, Numerical Solution of Partial Differential Equations, Cambridge University Press, Cambridge, 1996.
[23] D. Mumford, J. Shah, Optimal approximation by piecewise smooth functions and associated variational problems, Commun. Pure Appl. Math. 14 (1989) 577–685.
[24] S. Osher, J.A. Sethian, Fronts propagating with curvature-dependent speed: algorithms based on Hamilton–Jacobi formulations, J. Comput. Phys. 79 (1) (1988) 12–49.

[25] G. Papandreou, P. Maragos, Multigrid geometric active contour models, IEEE Trans. Image Process. 16 (2007) 229–240.
[26] A. Stuart, A.R. Humphries, Dynamical System and Numerical Analysis, Cambridge University Press, Cambridge, 1998.
[27] U. Trottenberg, C. Oosterlee, A. Schüller, Multigrid, Academic Press, London, 2001.
[28] L.A. Vese, T.F. Chan, A multiphase level set framework for image segmentation using the Mumford and Shah model, Int. J. Comput. Vis. 50 (3) (2002) 271–293.
[29] T.-T. Wua, Y.-F. Yang, Z.-F. Pang, A modified fixed-point iterative algorithm for image restoration using fourth-order PDE model, Appl. Numer. Math. 62 (2) (2012) 79–90.